Journal of Applied Physics

Acoustic topological valley transport with multimode edge states

Cite as: J. Appl. Phys. **130**, 124401 (2021); https://doi.org/10.1063/5.0058715
Submitted: 01 June 2021 . Accepted: 28 August 2021 . Published Online: 22 September 2021

Tianchong Wu, Xu Jiang, Xin Wu, Qiang Han, et al.

View Online Export Citation CrossMark

Challenge us.
What are your needs for periodic signal detection?
Watch
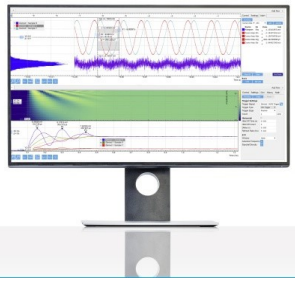
Zurich Instruments

© 2021 Author(s).

Journal of Applied Physics ARTICLE scitation.org/journal/jap

Acoustic topological valley transport with multimode edge states

Cite as: J. Appl. Phys. **130**, 124401 (2021); doi: 10.1063/5.0058715
Submitted: 1 June 2021 · Accepted: 28 August 2021 ·
Published Online: 22 September 2021

View Online Export Citation CrossMark

Tianchong Wu, Xu Jiang, Xin Wu, and Qiang Han[a)]

AFFILIATIONS

Department of Engineering Mechanics, School of Civil Engineering and Transportation, South China University of Technology, Guangzhou, Guangdong Province 510640, People's Republic of China

[a)]**Author to whom correspondence should be addressed:** emqhan@scut.edu.cn

ABSTRACT

Acoustic transport through topological edge states in phononic crystals improves the suppression of backscattering, which gives these systems significant potential for controlling sound waves. Recent research shows that only one acoustic edge state caused by topological valley phases can transmit in phononic crystals. This paper proposes a genre of valley phases with one, two, and three topological edge states created by transforming the structure of unit cells. The bulk-edge correspondence indicates that these edge states are topological based on the topological invariant number (i.e., the valley Chern number of one, two, and three) of this system coinciding with the number of topological edge states. Different types of defects are introduced into the phononic crystals, whose transmission spectra show that they can withstand bending defects. These results indicate that these systems have significant potential for application in noise control, acoustic communication, and acoustic-electrical integration.

Published under an exclusive license by AIP Publishing. https://doi.org/10.1063/5.0058715

I. INTRODUCTION

Recent years have seen the widespread use of the mathematical concept of topology in condensed-matter physics, leading to several interesting topological effects, such as the quantum Hall effect,[1–6] the quantum spin Hall effect,[7–14] and the quantum valley Hall effect (QVHE).[15–25] By studying topological insulators[26] in electronic systems, the present work extends research into the protected topological edge states (TESs) to other fields of physics such as photonics[27,28] and phononics.[29–32] Recent research has been seeking new phononic topological phases and has established TESs, which allow us to guide sound waves, overcome backscattering, and withstand defects.

Symmetry plays a key role in the generation of edge states in phononic topological phases. For example, to establish a one-way edge channel, a ring of circulating fluid is introduced in phononic crystals (PCs) with a triangular lattice[3] structure to break the time-reversal (TR) symmetry and simulate the quantum Hall effect, which is difficult to achieve in practice because of the complexity of fabricating annular waveguides. Similarly, the QVHE, which is marked by the band structure (BS) of the energy extremum in momentum space, is achieved by introducing a valley degree of freedom.[33–35] By breaking space-inversion symmetry in systems in which TR symmetry is fixed and the Chern number is zero, topologically nontrivial properties are generated that are attractive for transferring and storing information. Along these lines, Yang *et al.*[36] proposed two-dimensional periodic acoustic resonant cavity structures with topology QVH phases. They also discuss in detail topological valley states in non-Hermitian artificial acoustic structures[37] and topological valley transport of interlayer coupling and interlayer polarization[23,38] in double-layer PCs. However, only a single TES may be produced by the QVHE, which motivates us to study herein whether multiple TESs may be naturally produced in PC systems.

This work proposes a PC with an adjustable unit-cell configuration, allowing the number of TESs to vary from one to three depending on the geometric parameters of the unit cell. The unit-cell structure is formed by six rods aligned parallel to each other and that forms in the cross-sectional plane, a hexamer. The number of TESs is then varied by expanding or shrinking the hexamers by modifying the distance between rods. As a result, the PCs have C_3 symmetry, which lead to Dirac cones with accidental degeneracy.[39] QVH phases are then obtained by breaking the Dirac points. According to the bulk-edge correspondence,[40,41] the topological invariance of the system—the valley Chern number (VCN) $|C_v|$—is calculated to determine the number of TESs, and the Berry

Published under an exclusive license by AIP Publishing

curvature (BC) of the rhombohedral Brillouin zone (BZ) characterizes these new QVH phases.

The robustness of the PCs is investigated by introducing different types of defects. In the simulation, these topological phases can withstand bending defects, whereas backscattering occurs upon introducing disorders and cavities. PCs with multiple TESs are useful for broadening available phases in acoustic communication, thereby significantly increasing the number of transmission channels of topological states, which should help the development of multimode one-way waveguides and acoustic devices.

II. MODEL AND METHODS

A. Model of two-dimensional phononic crystals

PCs consist of artificial molecules, as shown in Fig. 1(a). Each unit cell contains six rods made up of soft, isotropic material in air to form a hexamer. The cylindrical rods of diameter d are arranged in a hexagonal lattice with lattice constant a, where $d = 4$ cm and $a = 5\sqrt{3}\,d/2$. The rod center is a distance R from the unit-cell center, and the velocity and the density of the background air are $c_{\text{air}} = 343$ m/s and $\rho_{air} = 1.21$ kg/m^3, respectively, and the velocity and the density of the soft-material rod are $c_{\text{rod}} = 100$ m/s and $\rho_{\text{rod}} = 1.21$ kg/m^3, respectively. In practice, aerogel[42] or Helmholtz resonators[43] are normally used to obtain an ideal soft acoustic medium in our simulation.

Unlike ordinary honeycomb unit cells, the entire hexamer is confined in a regular hexagonal unit cell for expansion or shrinkage. The red dashed line in Fig. 1(c) is the dispersion curve for the BS at $R = a/3$, as calculated by the pressure acoustics module of COMSOL Multiphysics with the Floquet boundary condition applied in the unit cell. A Dirac point appears in the BS at a frequency of 1650.5 Hz, which is a general point in k, in contrast with

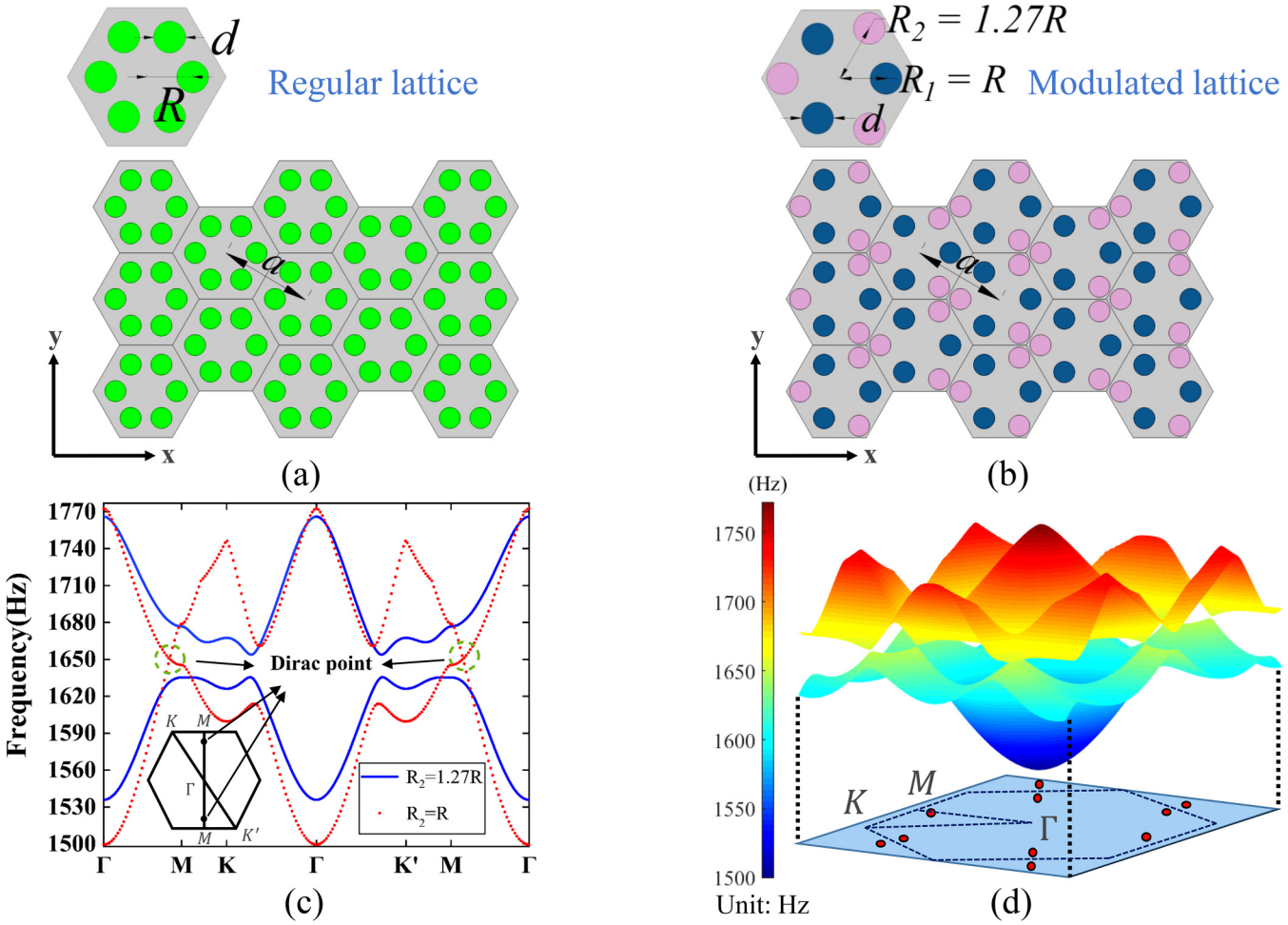

FIG. 1. (a) Schematic of hexagonal PC structures with a regular lattice structure. Hexamer unit cells contain six soft-material rods in air. (b) Schematic of hexagonal PC structures with modulated lattice and unit cells, in which $R_2 = 1.27\,R$, whereas $R_1 = R$. (c) BS of two different unit cells. The red dashed line is the dispersion curve of the regular lattice, and the black solid line is the dispersion curve of the modulated lattice. A pair of energy valleys appears at a general point. (d) Three-dimensional BS of PC with regular lattice. BZ contains three pairs of Dirac points.

Published under an exclusive license by AIP Publishing

other works that report Dirac points at high-symmetry points.[15–25] Compared with the ordinary honeycomb lattice model, we rotate the hexamer in the unit cell by $\pi/6$ so that the structure changes from honeycomb to hexagonal, which makes the Dirac point shift from the Γ point to a general point in the wave vector space. As shown in Fig. 1(d), the first BZ contains three pairs of Dirac points due to system symmetry. The Dirac point does not present at a high-symmetry point has also been studied.[44] To determine the valley degree of freedom, we must determine the energy valley, which is done by breaking the Dirac points, which equates to breaking the TR symmetry or space-inversion symmetry of the system. For sound wave, it is a longitudinal wave without spin or magnetoacoustic effect, and, thus, it cannot break the TR symmetry by applying external magnetic field while a ring of circulating fluid is too complicated to be applied.

Here, Dirac points are broken by breaking the space-inversion symmetry of the system. The hexamer composed of six rods can be regarded as composed of two trimers, marked in blue and pink in Fig. 1(b). The procedure to break the space-inversion symmetry is plotted in Figs. 1(a) and 1(b): the regular lattice modulated so that the mirror symmetry is broken and the rotational symmetry changes from C_6 to C_3. A Dirac point opens to form a complete bandgap, as shown by the black solid line in Fig. 1(c), and the valleys appear at a general point (i.e., non-high-symmetry point) in the momentum space. However, these valleys are different from those in previous reports.[15–25]

B. Number of topological edge states

To show the difference from the previous reports, we calculate the number of topological edge states at the interface in this valley phase. First, we construct a zigzag-type domain wall, which is the boundary between two PCs with different arrangements. The PCs are mirror-symmetric about this boundary. The PCs in the two domains have the same geometric parameters [see Fig. 2(a)] $R_1 = R$ and $R_2 = 1.27R$ but the hexamer in one of the domains is rotated by $\pi/3$ so that the blue-rod trimer of one domain takes the place of the pink-rod trimer of the opposite domain. Thus, acoustic waves are transmitted across the domain boundary without back-scattering. The projected BS of the stripped PCs is obtained by simulation. Surprisingly, as shown in Fig. 2(b), three TESs appear in the bandgap, where the edge modes at points A–C of the projected BS are plotted in Fig. 2(c). The pressure field is nonzero near this boundary and decays rapidly with distance from the domain wall. These three TESs are analyzed in Sec. II C.

C. Calculating the valley Chern number

To prove that multiple TESs can exist in this system, we must calculate the topological invariant number (topological VCN). The bulk-edge correspondence is confirmed by analytically solving the boundary problem, and the number of TESs between two topological domains equals the difference between the numbers of the

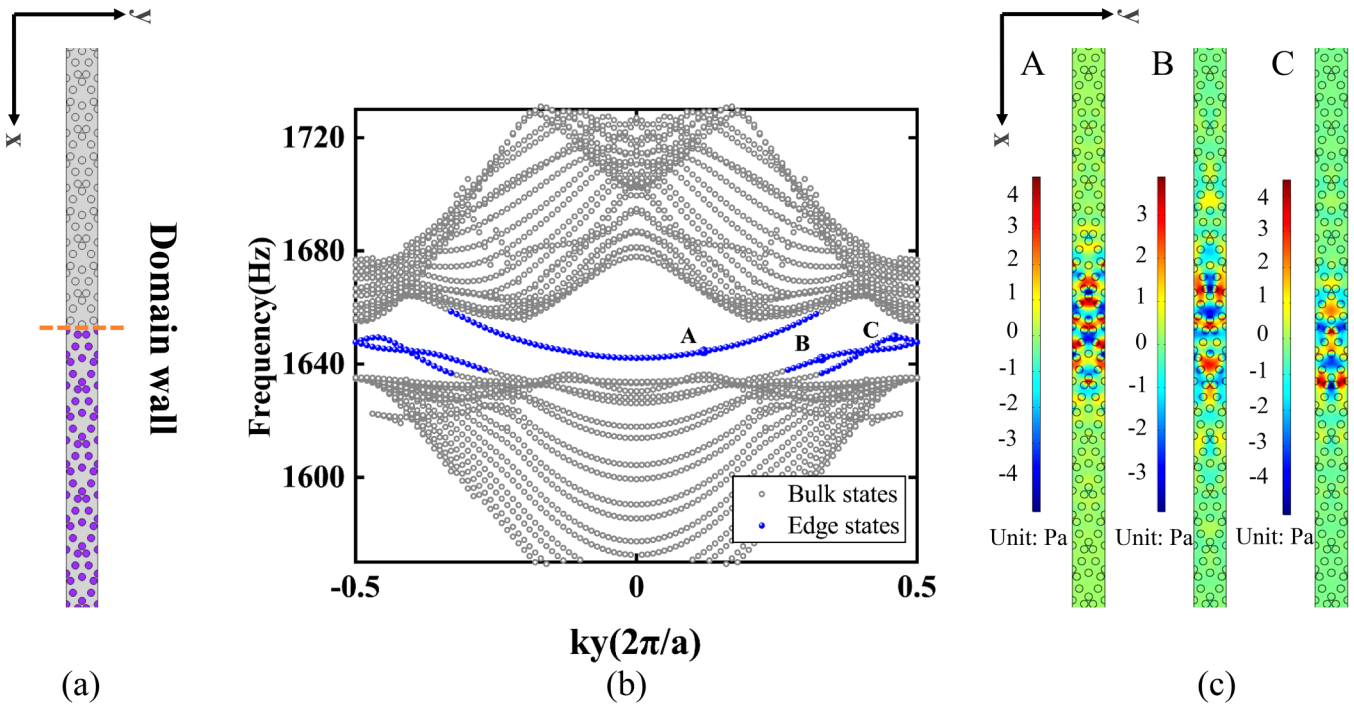

FIG. 2. TESs of PCs when $R_2 = 1.27\,R$ and $R_1 = R$. (a) Domain wall in stripped PC. (b) Projected BS of $R_2 = 1.27R$ at the $K(K')$ point. (c) Distributions of the pressure field near the domain wall at given points in the projected BS.

Published under an exclusive license by AIP Publishing

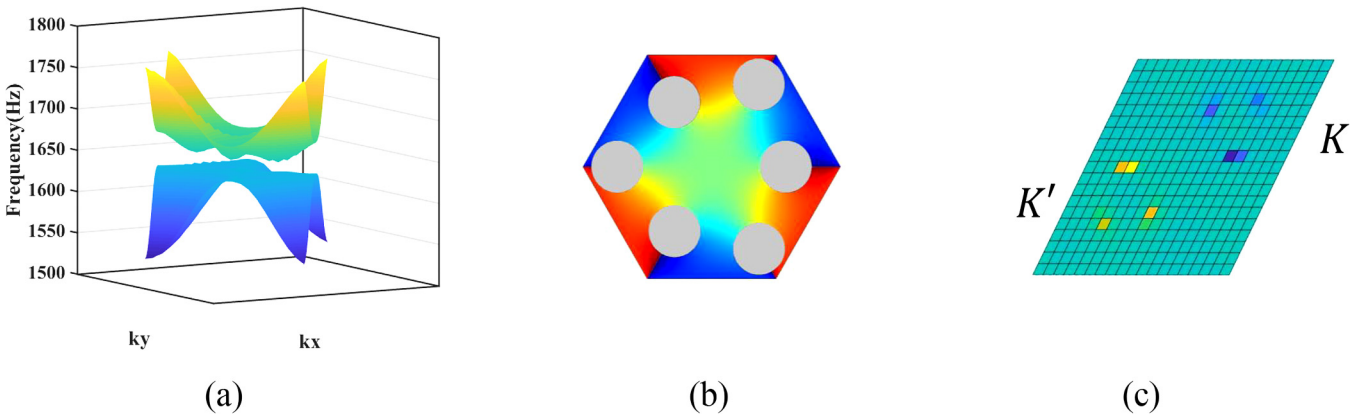

FIG. 3. (a) Three-dimensional BS of PCs with $R_2 = 1.27\,R$ and $R_1 = R$. (b) Phase diagram. (c) Corresponding BC in rhombus BZ where large peaks exist around K and K' points.

VCN crossing the boundary. The VCN of band n is defined by[45,46] where $F_{12}(k)$ is the BC defined by

$$c_n = \frac{1}{2\pi i}\int_{T^2} d^2k F_{12}(k), \tag{1}$$

$$F_{12}(k) = \partial_1 A_2(k) - \partial_2 A_1(k), \tag{2}$$

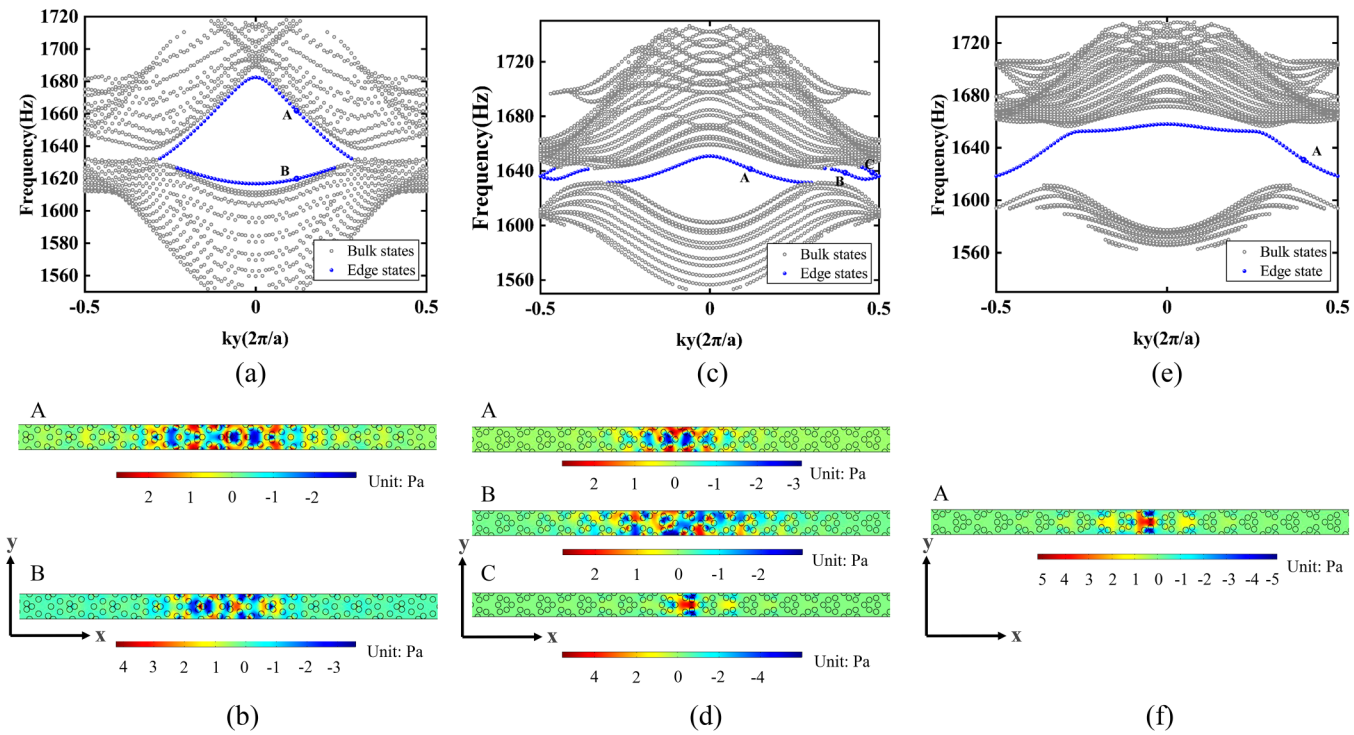

FIG. 4. TESs of PCs when $R_1 = R$ and for various values of R_2: (a), (c), and (e) projected BSs for $R_2 = 1.33\,R$, $R_2 = 0.71\,R$, and $R_2 = 0.63\,R$, respectively, at point K (K'). (b), (d), and (f) Distributions of pressure field near the domain wall at the given points in the projected BS.

Published under an exclusive license by AIP Publishing

where $A_\mu(k)$ ($\mu = 1, 2$) is the Berry connection defined by

$$A_\mu(k) = \langle n(k)|\partial_\mu|n(k)\rangle, \tag{3}$$

where $|n(k)\rangle$ is the nth normalized eigenstate of the PC imposing the Bloch wave vector k and the partial derivative ∂_μ stands for $\partial/\partial k_\mu$. The VCN is calculated by using a direct, universal method based on the finite-element method, whereby the BZ is divided into small zones.[47] Given that the first BZ in the PC structure is hexagonal, it is difficult to determine parallelogram meshes that cover the entire BZ directly. However, we can scan the rhombus zone containing points K and K' by using the following approach:

$$k_x = \frac{2\pi}{3a}(x+y), \quad k_y = \frac{2\pi\sqrt{3}}{3a}(x-y), \quad x = [0, \ldots, 1], \quad y = [0, \ldots, 1]. \tag{4}$$

The rhombus BZ can then be divided into uniform parallelogram meshes. Figures 3(a) and 3(b) show the three-dimensional (3D) BS and phase diagram of the pressure field, in which sound velocity, density, total-pressure field, and eigenfrequency are determined by simulation.

Figure 3(c) plots the BC of the rhombus BZ with the yellow (blue) points representing the upward (downward) peaks at $R_2 = 1.27R$. In this rhombus zone, the VCN can be easily determined by counting the number of peaks because the contribution of each peak of BC to the VCN is $|C| = 1/2$. Figure 3(c) shows three upward (downward) peaks at point K' (K) with the upward peaks of identical magnitude as the downward peaks in the BZ, so the Chern number is zero because of the preservation of the TR symmetry of the system. However, the VCN of the lower band (i.e., $C_v = C_k - C_{k'} = -3/2 - 3/2 = -3$) switches from -3 to $+3$ upon rotating the hexamer by $\pi/3$ about the center of the unit cell, so three TESs exist for acoustic transport along the domain wall separating these two types of unit cells, which is consistent with the results of our simulation.

III. RESULTS AND DISCUSSION

A. Valley phases for different unit-cell configurations

The number of TESs of the PC depends on the valley phase, and the appearance of different valley phases is determined by the

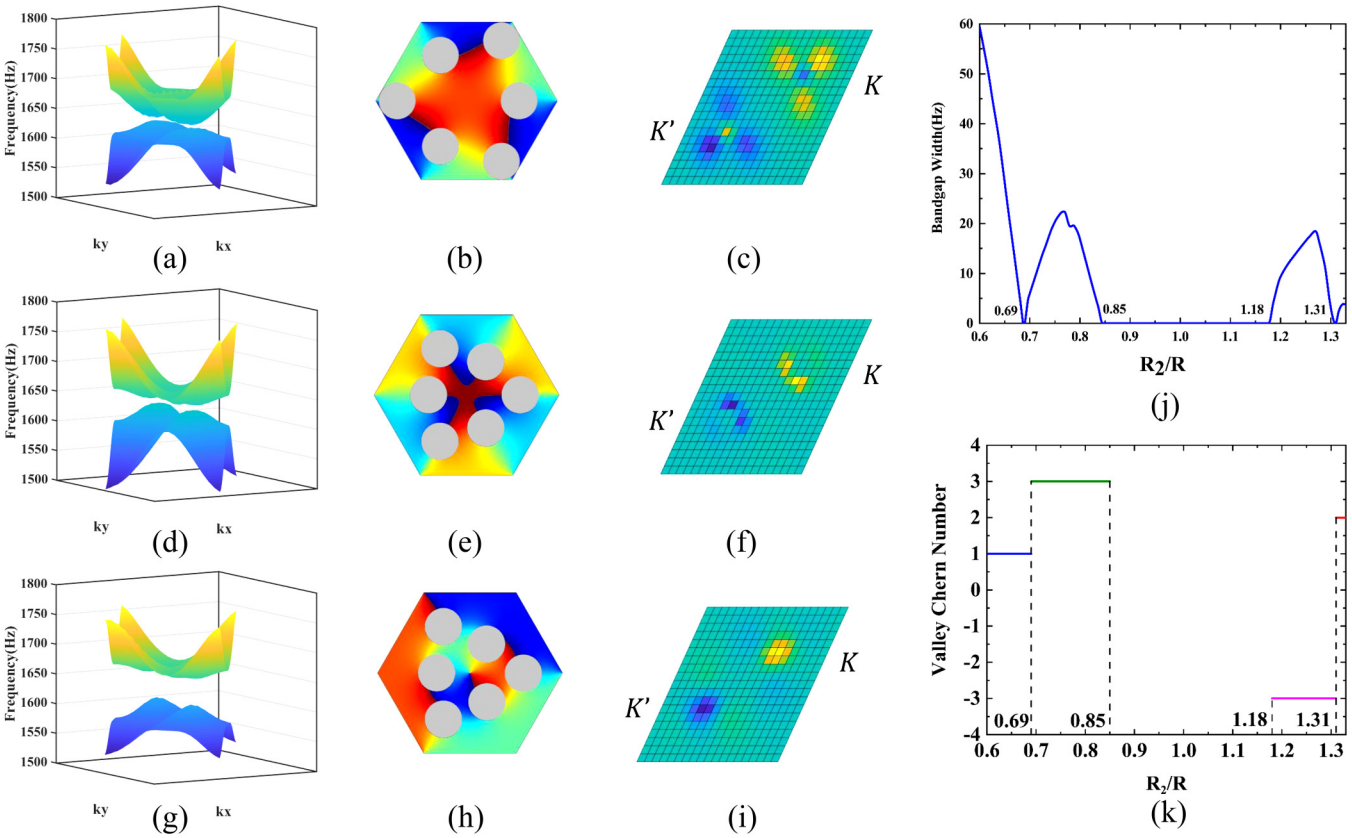

FIG. 5. (a), (d), and (g) Three-dimensional BS of PC when $R_2 = 1.33R$, $R_2 = 0.71R$, and $R_2 = 0.63R$ with $R_1 = R$. (b), (e), and (h) Phase diagram. (c), (f), and (i) Corresponding BC in rhombus BZ. $R_2 = 1.33R$ and $C_v = +2$; $R_2 = 0.71R$ and $C_v = +3$; and $R_2 = 0.63R$ and $C_v = +1$. (j) Variation of complete bandgap width associated with variation in R_2 with R_1 fixed where bandgap opens and closes multiple times. (k) Variation of VCN associates with varying R_2 with R_1 fixed where C_v can be -3, $+1$, $+2$, or $+3$.

Published under an exclusive license by AIP Publishing

scaling of the pink subset of rods. In the simulation, the blue subset of rods was fixed at $R_1 = R$, meanwhile, the pink subset is varied over $R_2 = 0.63\,R$, $R_2 = 0.71\,R$, $R_2 = 1.27\,R$, and $R_2 = 1.33\,R$, causing complete bandgaps to open and energy valleys to appear in BS. Figure 4 shows the projected BS of the stripped PCs with various R_2 values and the distribution of the pressure field of the TES eigenmodes at selected points.

Once again, similar to what happens for $R_2 = 1.27\,R$, a domain wall separates the two domains of PCs with identical geometric parameters. Upon expanding the pink subset to $R_2 = 1.33\,R$, two TESs appear inside the bandgap [see Fig. 4(a)], and the edge states at points A and B are shown in Fig. 4(b). The pressure field is nonzero only near the domain wall and decays rapidly with distance from the domain wall. Similarly, upon shrinking the pink subset to $R_2 = 0.71\,R$, three TESs appear again in the bandgap as shown in Figs. 4(c) and 4(d). When $R_2 = 0.63\,R$, only one TES appears in the bandgap, as shown in Figs. 4(e) and 4(f).

We now calculate the VCN of the PCs. Figures 5(a), 5(b), 5(d), 5(e), 5(g), and 5(h) show the 3D BS of a rhombic BZ and the phase diagram. Figures 5(c), 5(f), and 5(i) show the BC of the lower band for the rhombus BZ. Given the preservation of TR symmetry, the upward and downward peaks in the BZ are identical and the Chern number is zero, whereas the BC near the points $K(K')$ is not zero and produces large peaks. The band is characterized by a variable VCN with radius R_2. Figure 5(c) shows the BC for the rhombus BZ at $R_2 = 1.33\,R$ (expansion of the pink subset), where $C_v = C_k - C_{k'} = +2$, as determined by counting the number of peaks. When $R_2 = 1.27R$, the pressure field indicating the blue and pink rods can be considered as a large trimer and a small trimer at different positions within the unit cell, forming two different sublattices. If the pink subset is shrunk to $R_2 = 0.71\,R$, the large and small trimers would exchange positions within the unit cells, so the upward and downward peaks at the K and K' points would swap, reversing the direction of acoustic transport. Thus, for $R_2 = 0.71\,R$, $C_v = C_k - C_{k'} = +3$. The coupling strength is enhanced by further shrinking the pink subset, so the hexamer can be regarded as a whole. When $R_2 = 0.63\,R$, a single peak appears at the points K and K' and $C_v = C_k - C_{k'} = +1$.

The band inversion occurring in the BS is related to different phases with several TESs, which could be identified by the opening–closing–reopening phenomenon of a complete bandgap. The several disappearances and appearances of the complete bandgap, leading to the variation of the VCN shown in Fig. 5(k), are plotted in Fig. 5(j), where R_1 is fixed while R_2 varies. During the expansion of pink rods, a Dirac point is observed when $R_2 = R$; as R_2 increases, the complete bandgap opens when $R_2 = 1.18\,R$ and closes when $R_2 = 1.31\,R$, where the VCN is -3, associated with three TESs. We then increase R_2 continuously to $1.33\,R$, which is the threshold of R_2 in this experiment for geometry limitation, and the gap opens gradually, where the VCN is $+2$, associated with two TESs. Similarly, as the pink rods shrink, R_2 decreases and the gap opens at $R_2 = 0.85\,R$. The gap suddenly closes and reopens when $R_2 = 0.69\,R$, where the VCN is $+3$, associated with three TESs. We then decrease R_2 continuously, and the gap opens gradually so the six rods may be considered as a whole, where the VCN is $+1$, associated with one TES.

B. Results of robustness

Next, we investigate by simulation the most important physical characteristic of a valley Hall insulator in which large-scale defects modify the valley vortex chirality and cause different topological valley transport and backscattering and a topological robustness against defects. As shown in Fig. 6, we first calculate the four types of transmission spectra for linear acoustic transport without defects. The frequency band of one-way acoustic transport resulting from different valley states depends on R_2, so by tuning R_2 of the subset of pink rods, we can obtain the desired frequency band of one-way acoustic transport.

We now introduce four groups with different lattice-scale defects to explore the system robustness [see Fig. 7(a)]. The defects

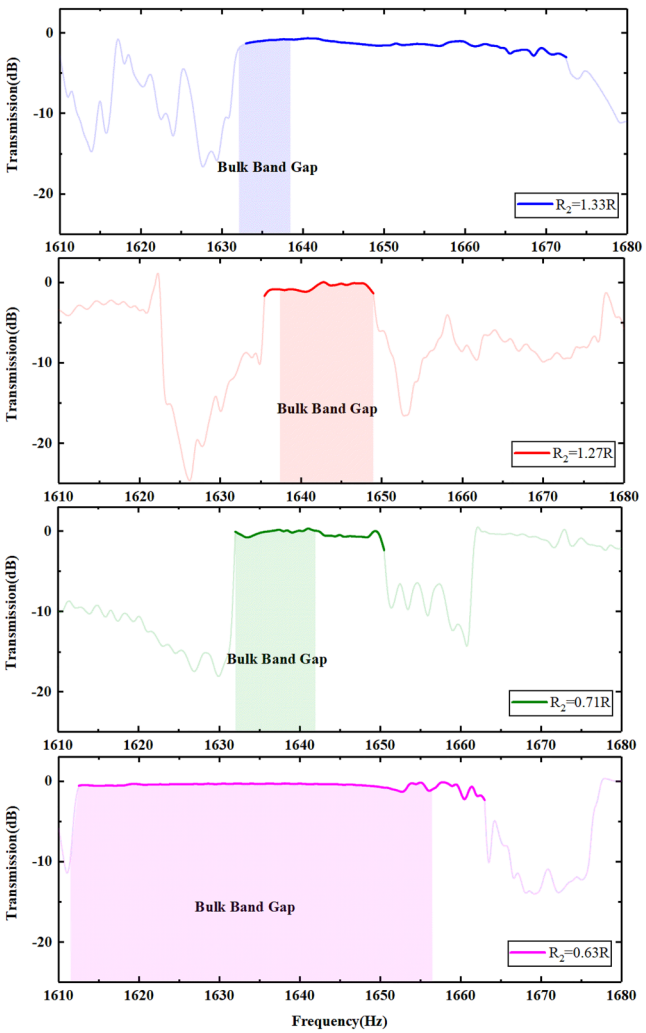

FIG. 6. Transmission spectra of uninterrupted linear acoustic transport of different R_2 values, corresponding to different bands of acoustic transport frequency, and the dashed area represents the bulk bandgap.

Published under an exclusive license by AIP Publishing

take the following form: (1) a Z-shaped bending defect with sharp corners, (2) a trapezoidal bending defect with corners, (3) disorders defects caused by randomly changing the angle of the hexamer at both ends of the boundary, and (4) cavity defects caused by removing some hexamers. For example, when $R_2 = 0.63\,R$, Fig. 7(b) shows the simulation of the absolute pressure field distribution under the above situations. Compared with the field distribution without defects, the reflection caused by various bending defects is very weak, and the valley edge states guide the sound wave to smoothly bypass the sharp bends.

However, upon introducing severe disorders and cavity defects, these large-scale defects cause backscattering, whereby acoustic waves are strongly reflected upon encountering defects. For $R_2 = 0.63\,R$, the introduction of different types of defects produces the transmission spectrum of the topological acoustic waveguide as shown in Fig. 7(b). Within the full TES frequency band domain, the waveguide transmissivity of the sample with bending defects is almost the same as that of the sample without defects. Upon adding disorders and cavity defects, the transmissivity suddenly decreases or increases, which is indicative of reflections within the waveguide. This is consistent with the results in the simulation field distribution diagram.

Given Z-bends and trapezoid-bends, the zigzag-edge-type domain wall remains such that the bending-defect transmissivity remains almost the same as that of a straight waveguide without defects. One difference caused by the bending defects is that, upon introducing lattice-size disorders and cavity defects, the zigzag-type boundary is broken, which means that the acoustic wave is transmitted across the entire boundary, meaning that the boundary no longer exists. In certain frequency bands, the acoustic wave undergoes distinct reflections when bending defects are introduced in the acoustical waveguide, further decreasing and increasing the transmissivity, as shown in Fig. 7(b).

To summarize, in a topological acoustic waveguide based on the topological QVH phase change, bending defects cause trivial backscattering, whereas large-scale defects such as disorders and cavities lead to intervalley scattering and thereby reduce the transmissivity. Moreover, a balance exists between structural simplicity

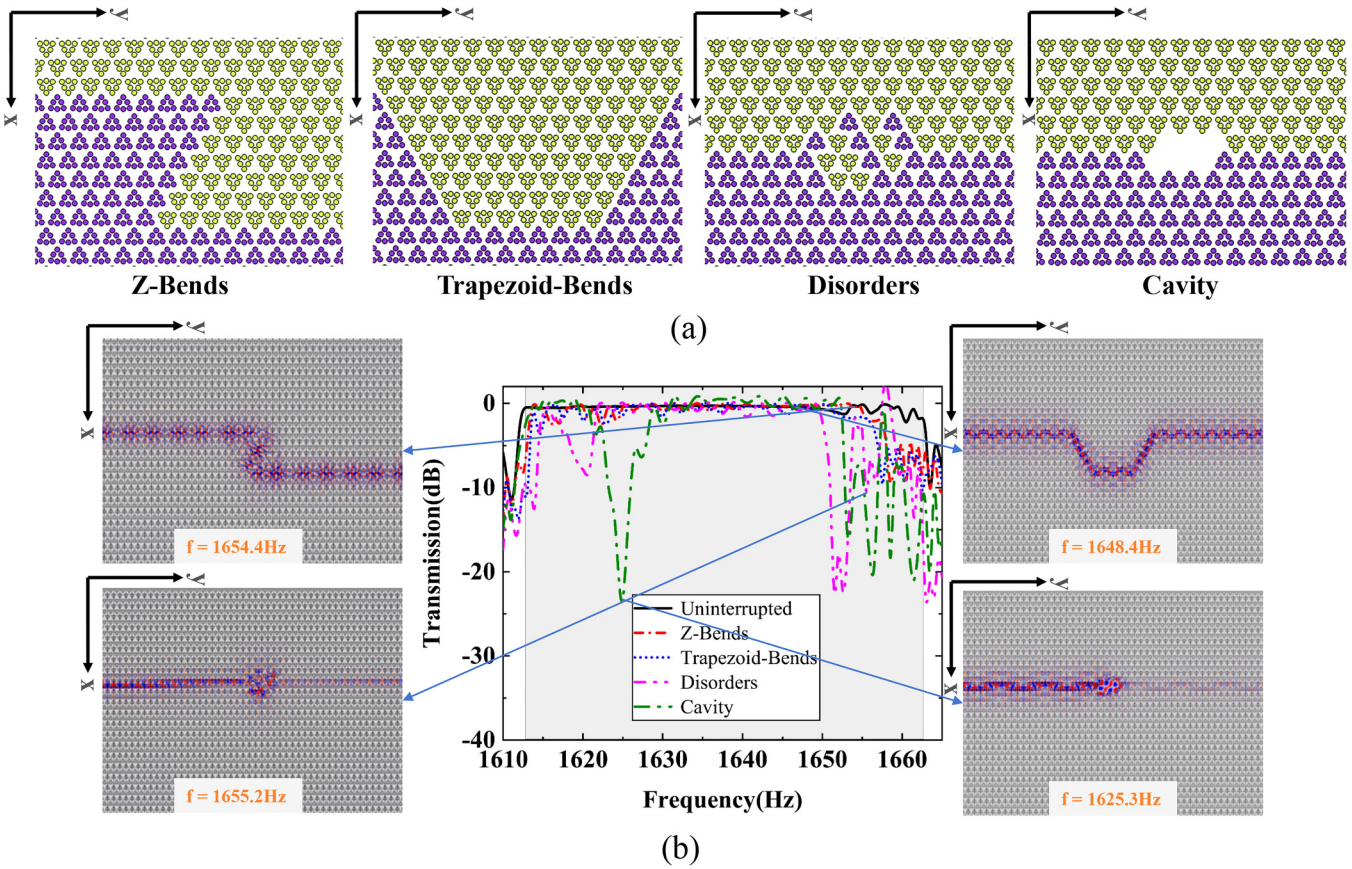

FIG. 7. (a) Schematic representation of Z-bends, trapezoid-bends, disorders, and cavity defects. (b) Transmission spectrum for $R_2 = 0.63\,R$. Simulated pressure field distributions of four different defects are inserted. The various bending defects cause a very weak reflection but the transmissivity suddenly decreases or increases when disorders and cavity are introduced.

Published under an exclusive license by AIP Publishing

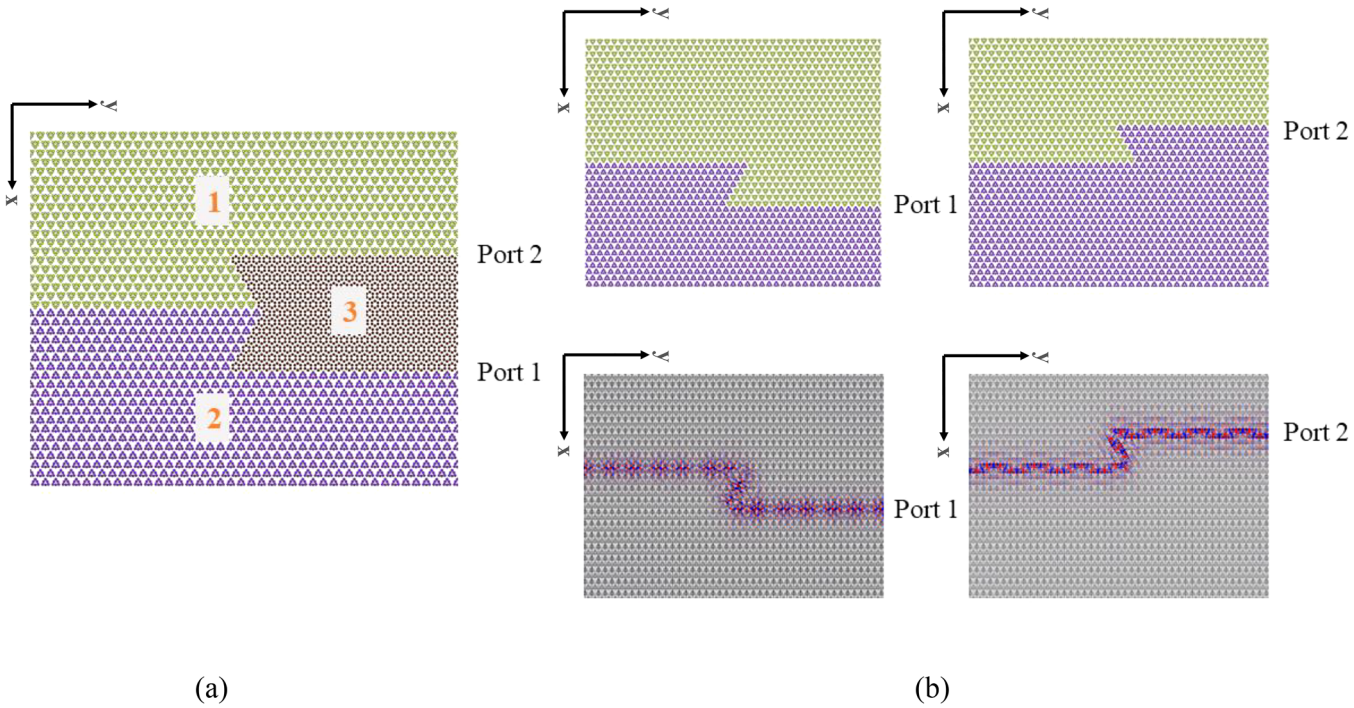

FIG. 8. (a) Schematic of operation of reconfigurable TESs in which R_1 and R_2 of zones 1–3 are all adjustable. (b) Pressure field distribution when controllable zone 3 is converted between two different topological structures.

and robustness; in other words, the implementation of the topology valley transport structure is simpler and more convenient to control accomplished with weaker robustness to defects.

C. Application prospects

The reconfigurability of the structure is the basis of the current application of functional acoustic devices and acoustic metamaterials. Figure 8(a) presents a conceptual topology conversion acoustic waveguide. The hexamer units in the zone are all connected to an electric motor. The path of the topology-protected edge states is easily adjusted by changing the radius R_1 of the blue set of rods and the radius R_2 of the pink set of rods in zone 3. The sound wave exits from ports 1 or 2 along different paths, as shown in Fig. 8(b), because the hexamer is easily adjusted, and the range of zone 3 is also controllable. By adjusting R_1 and R_2 of zones 1 and 2, the frequency band and the channel mode of acoustic wave transport can be adjusted to realize the acoustic devices with multiple adjustment functions.

In electronics, structures with multiple TESs and a large VCN will have circuit interconnects with greatly reduced contact resistance. For photonic applications, the mode density and coupling efficiency are increased in multimode one-way waveguides and "one-way photonic circuits" can be designed where the number of one-way waveguide modes equals the gap Chern number at the interface.[28] However, such similar researches are relative rare in phononics. In our study, the specific topological insulator with varied VCN could be obtained by changing the unit-cell structure, in which the changes in the number of edge states may be helpful to achieve similar functions in phononic applications.

IV. CONCLUSION

We propose and simulate a QVH phase in a two-dimensional PC with large VCN. The PC is composed of hexamers made of rods of soft material. Simply expanding or shrinking a group of rods in the hexamer produces 1, 2, and 3 TESs, which is confirmed by calculating the topological VCN of the system according to the bulk-edge correspondence. The system is shown to be sufficiently robust against bending defects for use as a bending waveguide but moderately robust against disorders and cavity defects on the lattice scale. In addition, we calculate the transmission spectra. By exploiting the adjustability of the hexamer lattice structure, the robustness of the TESs against bending defects, and the multimode nature of the waveguide, we designed a reconfigurable topological acoustic channel-mode waveguide with an adjustable frequency band. This device opens new opportunities for acoustic topological valley transport and "one-way phononic circuits."

ACKNOWLEDGMENTS

The authors wish to acknowledge the support from the Natural Science Foundation of China (Grant Nos. 11772130 and

Published under an exclusive license by AIP Publishing

11902117) and the Basic and Applied Basic Research Project (Grant No. 202002030367).

DATA AVAILABILITY

The data that support the results of this paper are available from the corresponding author upon reasonable request.

REFERENCES

[1]R. Fleury, D. L. Sounas, C. F. Sieck, M. R. Haberman, and A. Alù, Science **343**, 516 (2014).
[2]A. B. Khanikaev, R. Fleury, S. H. Mousavi, and A. Alù, Nat. Commun. **6**, 8260 (2015).
[3]Z. Yang, F. Gao, X. Shi, X. Lin, Z. Gao, Y. Chong, and B. Zhang, Phys. Rev. Lett. **114**, 114301 (2015).
[4]X. Ni, C. He, X.-C. Sun, X.-P. Liu, M.-H. Lu, L. Feng, and Y.-F. Chen, New J. Phys. **17**, 053016 (2015).
[5]Z.-G. Chen and Y. Wu, Phys. Rev. Appl. **5**, 054021 (2016).
[6]A. Souslov, B. C. van Zuiden, D. Bartolo, and V. Vitelli, Nat. Phys. **13**, 1091 (2017).
[7]J. Mei, Z. Chen, and Y. Wu, Sci. Rep. **6**, 32752 (2016).
[8]C. L. Kane and E. J. Mele, Phys. Rev. Lett. **95**, 226801 (2005).
[9]B. A. Bernevig, T. L. Hughes, and S.-C. Zhang, Science **314**, 1757 (2006).
[10]Y. Deng, H. Ge, Y. Tian, M. Lu, and Y. Jing, Phys. Rev. B **96**, 184305 (2017).
[11]S. Yves, R. Fleury, F. Lemoult, M. Fink, and G. Lerosey, New J. Phys. **19**, 075003 (2017).
[12]C. He, S.-Y. Yu, H. Ge, H. Wang, Y. Tian, H. Zhang, X.-C. Sun, Y. B. Chen, J. Zhou, M.-H. Lu, and Y.-F. Chen, Nat. Commun. **9**, 4555 (2018).
[13]D. Jia, H. Sun, J. Xia, S. Yuan, X. Liu, and C. Zhang, New J. Phys. **20**, 093027 (2018).
[14]L. Xu, H.-X. Wang, Y.-D. Xu, H.-Y. Chen, and J.-H. Jiang, Opt. Express **24**, 18059 (2016).
[15]T.-W. Liu and F. Semperlotti, Phys. Rev. Appl. **9**, 014001 (2018).
[16]T.-W. Liu and F. Semperlotti, Phys. Rev. Appl. **11**, 014040 (2019).
[17]J. Lu, C. Qiu, L. Ye, X. Fan, M. Ke, F. Zhang, and Z. Liu, Nat. Phys. **13**, 369 (2016).
[18]B.-Z. Xia, T.-T. Liu, G.-L. Huang, H.-Q. Dai, J.-R. Jiao, X.-G. Zang, D.-J. Yu, S.-J. Zheng, and J. Liu, Phys. Rev. B **96**, 094106 (2017).
[19]X. Ni, M. A. Gorlach, A. Alu, and A. B. Khanikaev, New J. Phys. **19**, 055002 (2017).
[20]X. Wen, C. Qiu, J. Lu, H. He, M. Ke, and Z. Liu, J. Appl. Phys. **123**, 091703 (2018).
[21]X. Liu, Q. Guo, and J. Yang, Appl. Phys. Lett. **115**, 074102 (2019).
[22]L. Ye, C. Qiu, J. Lu, X. Wen, Y. Shen, M. Ke, F. Zhang, and Z. Liu, Phys. Rev. B **95**, 174106 (2017).
[23]J. Lu, C. Qiu, W. Deng, X. Huang, F. Li, F. Zhang, S. Chen, and Z. Liu, Phys. Rev. Lett. **120**, 116802 (2018).
[24]Z.-G. Geng, Y.-G. Peng, Y.-X. Shen, D.-G. Zhao, and X.-F. Zhu, Appl. Phys. Lett. **113**, 033503 (2018).
[25]H. Dai, J. Jiao, B. Xia, T. Liu, S. Zheng, and D. Yu, J. Phys. D: Appl. Phys. **51**, 175302 (2018).
[26]M. Z. Hasan and C. L. Kane, Rev. Mod. Phys. **82**, 3045 (2010).
[27]X. Xi, K.-P. Ye, and R.-X. Wu, Photonics Res. **8**, B1 (2020).
[28]S. A. Skirlo, L. Lu, and M. Soljačić, Phys. Rev. Lett. **113**, 113904 (2014).
[29]R. Süsstrunk and S. D. Huber, Science **349**, 47 (2015).
[30]S. H. Mousavi, A. B. Khanikaev, and Z. Wang, Nat. Commun. **6**, 8682 (2015).
[31]C. He, X. Ni, H. Ge, X.-C. Sun, Y.-B. Chen, M.-H. Lu, X.-P. Liu, and Y.-F. Chen, Nat. Phys. **12**, 1124 (2016).
[32]L. Fan, Y. He, X. Chen, and X. Zhao, Appl. Phys. Express **13**, 017004 (2020).
[33]A. Rycerz, J. Tworzydło, and C. W. J. Beenakker, Nat. Phys. **3**, 172 (2007).
[34]D. Xiao, W. Yao, and Q. Niu, Phys. Rev. Lett. **99**, 236809 (2007).
[35]F. Zhang, A. H. MacDonald, and E. J. Mele, Proc. Natl. Acad. Sci. U.S.A. **110**, 10546 (2013).
[36]Y. Yang, Z. Yang, and B. Zhang, J. Appl. Phys. **123**, 091713 (2018).
[37]M. Wang, L. Ye, J. Christensen, and Z. Liu, Phys. Rev. Lett. **120**, 246601 (2018).
[38]M. Gao, S. Wu, and J. Mei, New J. Phys. **22**, 013016 (2020).
[39]J. Lu, C. Qiu, S. Xu, Y. Ye, M. Ke, and Z. Liu, Phys. Rev. B **89**, 134302 (2014).
[40]X.-L. Qi, Y.-S. Wu, and S.-C. Zhang, Phys. Rev. B **74**, 045125 (2006).
[41]R. S. K. Mong and V. Shivamoggi, Phys. Rev. B **83**, 125109 (2011).
[42]M. D. Guild, V. M. García-Chocano, J. Sánchez-Dehesa, T. P. Martin, D. C. Calvo, and G. J. Orris, Phys. Rev. Appl. **5**, 034012 (2016).
[43]N. Fang, D. Xi, J. Xu, M. Ambati, W. Srituravanich, C. Sun, and X. Zhang, Nat. Mater. **5**, 452 (2006).
[44]H. Cao and J. Mei, "Volume 13: Vibration, acoustics and wave propagation," in *Proceedings of the ASME 2014 International Mechanical Engineering Congress and Exposition, 14–20 November*. (Montreal, Quebec, Canada, 2014).
[45]D. Xiao, M.-C. Chang, and Q. Niu, Rev. Mod. Phys. **82**, 1959 (2010).
[46]T. Fukui, Y. Hatsugai, and H. Suzuki, J. Phys. Soc. Jpn. **74**, 1674 (2005).
[47]C. Wang, H. Zhang, H. Yuan, J. Zhong, and C. Lu, Front. Optoelectron. **13**, 73 (2020).

Published under an exclusive license by AIP Publishing